Earth Planet. Sci. Lett. 647 (2024) 119020

Contents lists available at ScienceDirect

Earth and Planetary Science Letters

journal homepage: www.elsevier.com/locate/epsl

The fate of ultramafic-rich mélanges in cold to hot subduction zones: Implications for diapirism (or not) and chemical geodynamics

Anna M. Rebaza [a,*], Ananya Mallik [a], Emily H.G. Cooperdock [b], Bridgett I. Holman [a]

[a] *Department of Geosciences, University of Arizona, 1040 E 4th St, Tucson, AZ 85721, United States*
[b] *Department of Earth, Environmental & Planetary Sciences, Brown University, United States*

ARTICLE INFO

Editor: Dr R. Hickey-Vargas

Keywords:
Subduction zones
Ultramafic mélange
Melting
Diapir
Dehydration

ABSTRACT

Buoyant ultramafic-rich (serpentine- or chlorite-rich) mélange diapirs in sediment-starved subduction zones can transport slab material to arc sources. While the buoyancy of chlorite-rich mélanges was previously investigated, serpentine-rich mélanges were never explored. Thus, the overall contribution of ultramafic-rich mélanges to buoyancy, the conditions for diapir formation, and their fate in subduction zones are not well constrained. Here, we investigate the partial melting behavior and the associated density transformations of a serpentine-rich matrix (5–10 wt.% H_2O) with minor sediments (9:1 ratio) at fore-arc (~65 km) to sub-arc (~95 km) depths (2–3 GPa and 800–1250 °C) and compare to that of chlorite-rich mélanges from the literature. Our results show that the solidus of serpentine-rich matrices is between 1050 and 1100 °C and requires either diapiric rise of the mélange into the hotter mantle wedge or interactions with a hotter asthenosphere through slab tears to partially melt and produce basaltic melts, whether in hot or cold slab channels. Chlorite-rich mélanges may account for the sources of some arc lavas, but partial melting of serpentine-rich mélanges produce melts depleted in CaO, TiO_2, alkalis, and are highly enriched in MgO compared to basaltic arc lavas. Both serpentine-rich and chlorite-rich matrices dehydrate to form denser peridotite and lose buoyancy at ~800 °C and ≥1000 °C, respectively. Even if diapirism initiates in such mélanges near the slab-mantle interface, they would likely lose buoyancy upon ascent into the hotter mantle wedge resulting in stalled or failed diapirs. Diapir growth (τa) is controlled by the interplay of density, thickness and viscosity of the mélange, as well as the timescale of slab subduction (τs) and thermal structure of the subduction zone. We observe that the onset of diapirs in cold subduction zones requires mélanges that may sometimes be thicker than that observed by field and geophysical studies, while hot subduction zones overall require thinner mélanges. Thus, ultramafic-rich mélange diapirs may occur but only under specific conditions and when the diapiric ascent timescale is faster than the thermal equilibration barrier of ~800–1000 °C (especially at the core of the mélange). Dehydration or partial melting of ultramafic-rich mélanges can affect the large ion lithophile element (LILE), volatiles, and high-field strength element (HFSE) budgets in the mantle wedge. Partial melting (caused by a diapiric rise or slab tear) does not fractionate LILEs from HFSEs at $T \geq 1100$ °C and if the mélange has a lower LILE/HFSE to begin with, that signature is transferred to arc sources. Dehydration releases aqueous fluids rich in fluid-mobile elements (LILE and volatiles) relative to HFSE. Thus, the characteristic high LILE/HFSE signature of aqueous fluids is transferred to arc magma sources. Given high LILE/HFSE ratio is a ubiquitous arc magma signature, but slab tears are not, and diapirism in ultramafic-rich mélanges is highly conditional, this study corroborates that aqueous fluids released from sediment-starved mélanges are the predominant mass transfer agents rather than diapirs.

1. Introduction

In addition to the classic concept that mass transfer from the slab to arc sources occurs through the release of aqueous fluids and partial melts (Elliott et al., 1997; Hawkesworth et al., 1997; Kessel et al., 2005; Miller et al., 1994), recent studies suggest that mélange diapirs (matrix + blocks) detached from the down-going slab may have profound implications on arc magma diversity, mantle heterogeneity, and deep Earth geochemical cycling (Codillo et al., 2018; Cruz-Uribe et al., 2018; Ducea et al., 2022; Marschall and Schumacher, 2012; Nielsen and Marshall,

---

* Corresponding author.
E-mail address: arebaza@arizona.edu (A.M. Rebaza).

https://doi.org/10.1016/j.epsl.2024.119020
Received 28 February 2024; Received in revised form 28 August 2024; Accepted 17 September 2024

2017).

The slab-mantle interface, known as the subduction channel or 'mélange' (Cloos and Shreve, 1988), is an important rheological boundary layer detected as a low-velocity seismic structure that extends from hundreds of meters to ~8 km thickness, and persists down to ~150 km depth (Abers et al., 2020; Zhang, 2020). Fossil-exhumed channels reveal a complex tectonic mixing of diverse high-pressure (HP) and ultra-high-pressure (UHP) rocks, chaotically embedded in a fine-grained and highly deformed matrix of predominantly ultramafic composition (e.g., Shreve and Cloos, 1986). The development of ultramafic-rich mélange channels can be restricted to sediment-starved trenches (Geersen, 2019), where hydrated fore-arc mantle rocks (e.g., Raia et al., 2022), hydrated abyssal peridotites (e.g., Butjosa et al., 2023), and subducted seamount rocks (Straub et al., 2015) are the predominant ultramafic protoliths with additional meta-mafic (Blanco-Quintero et al., 2011; Lázaro and García-Casco, 2008; Sorensen and Grossman, 1993) and meta-sedimentary blocks (Breeding et al., 2004; Spandler et al., 2008; Penniston-Dorland and Harvey, 2023). The crustal rocks can provide substantial aqueous fluids rich in Si, Mg, Ca, and Al (Walowski et al., 2015) as they are gradually absorbed into the matrix, producing a wide range of ultramafic compositions from serpentine (Mg-Fe) to chlorite-rich matrices (Si-Al-Ca). Hydrated ultramafic-rich matrices are well-suited to carry, transport, and exhume HP and UHP crustal blocks along subduction channels (Hermann et al., 2000) because they are rheologically weak (Cloos and Shreve, 1988; Grigull et al., 2012) and with low density (~2500–2600 kg/m^3) (Coleman, 1971) due to the presence of low density hydrous minerals (e.g., serpentine, chlorite) that host significant amounts of volatiles (e.g., H, N, O). However, it is not yet clear whether those ultramafic mélange matrices can preserve these properties as they subduct from forearc to subarc depths (~65–100 km), where diapir initiation likely occurs (Behn et al., 2011).

Geochemical observations on arc lavas (Nielsen and Marschall, 2017), geophysical observations on sphere-like scattering obstacles (Lin et al., 2021), geodynamic- and thermodynamic modeling and experimental petrology studies (Castro et al., 2010; Codillo et al., 2018; Cruz-Uribe et al., 2018; Gerya and Yuen, 2003) support the idea of mélange diapirs in subduction zones. However, the dominance of diapirs as an agent for slab material transportation to arc magma sources is still debated. Conversely, diapirism appears unsupported by seismic studies which demonstrate that crustal material can be carried beyond sub-arc depths nearly intact without significant mass loss in the Aleutians and Marianas slabs (Horleston and Helffrich,2012). The presence of diapirs would also affect temperature predictions using H_2O/Ce and H_2O/K geothermometers on arc lavas (Codillo et al., 2018; Hermann and Spandler, 2008), reflecting temperatures in the rising diapir rather than the slab-mantle interface. Moreover, partial melting of mélanges fluxed by hotter mantle or asthenosphere may not generally support the global high LILE/HFSE signatures observed in arc lavas worldwide (Kelemen et al., 1990). Indeed, HFSE-enrichment observed in arc rocks have been linked to slab tears, such as in the Central Apennine, Cocos, (e.g., Rosenbaum et al., 2008) and to mélange diapir melting (e.g., Liu et al., 2024). All these concerns indicate that mélange diapirs may be unique to specific slabs and are dependent on the slab-top geotherm (T), pressure (P) (Syracuse et al., 2010) and bulk composition of the mélange.

So far, previous studies have relied on thermodynamic modeling and endmember mineral densities to assess the buoyancy of chlorite-rich mélanges of diverse compositions (Codillo et al., 2023; Ho, 2019; Lakey and Hermann, 2022). But how serpentine-rich mélanges would contribute to mélange buoyancy and mass transfer (e.g., LILEs, volatiles, and HFSE) from fore-arc to sub-arc depths is not yet experimentally constrained. To address this, we: 1) Perform new piston-cylinder experiments to measure mineral transformations of serpentine-rich matrices in sediment-starved subduction channels from forearc to sub-arc regimes (2–3 GPa and 800–1250 °C). 2) Evaluate the capability of the thermodynamic software pMELTS to reproduce our reported experimental data on serpentine-rich bulk compositions at similar P-T conditions and the software's potential use for future studies. 3) Assess diapirism of a diverse suite of ultramafic-rich mélanges by exploring density contrasts relative to the overriding mantle at relevant P-T conditions and the interplay of mélange viscosity and thickness at different subduction rates. We then discuss the fate of these subducted ultramafic-rich mélanges and the potential chemical geodynamic scenarios for various element groups (e.g., LILES, volatiles, and HFSEs) in cold to hot subduction zones.

2. Starting material and methods

This study simulates the subduction of serpentine-rich matrices with minor sedimentary components, as observed in natural outcrops (Breeding et al., 2004; Penniston-Dorland and Harvey, 2023; Spandler et al., 2008). It is important to emphasize that the starting material used in this study can either represent the bulk composition of an ultramafic matrix (with some sediments mixed) or the bulk mélange composition of a serpentine-rich matrix with minor crustal blocks. Here, we used the bulk major composition of a subducted abyssal serpentinite from Kampos Belt in Syros (Cooperdock et al., 2018) and a shaly/pelitic material from San Simeon (Ukar and Cloos, 2019) as references, and combined them in the ratio of 9:1. Both natural mélange compositions represent subducted material at fore-arc depths, with maximum P-T peaks of ~2 GPa and ~500 °C for the serpentinite matrix (Trotet et al., 2001) and maximum P-T peaks of ~0.8 GPa and ~250 °C for shaly matrix (Platt, 2015; Sadofsky and Bebout, 2003). Our study material explores a composition with lower alkalis (0.5 wt.%), SiO_2/MgO (~1.2) and Al_2O_3/FeO (~0.4) and higher H_2O (5–10 wt.%) compared to prior studies on chlorite-rich mélanges and peridotite mantle fluxed by slab material or mélange material (Codillo et al., 2023, 2018; Ho, 2019; Lakey and Hermann, 2022; Mallik et al., 2016, 2015; Till et al., 2012) which show large variations in SiO_2/MgO (~1.2–4.2), alkalis (0.1 to ≥2 wt.%), Al_2O_3/FeO (~0.3–3.5) and H_2O contents (0–14.5 wt.%) (Figure S1). More detail on the compositions of the natural mélange matrices used as references, the starting materials in this study, and starting materials in previous studies are reported in Table S1.

All experiments were carried out using half-inch assemblies in piston-cylinder devices at the Experimental Petrology Laboratory at the University of Arizona. One set of reverse heating experiments was performed at 2 GPa at a temperature range of 800 to 1250 °C and the second set was performed at 3 GPa from 1000 to 1250 °C, which correspond to deep forearc (~65 km) and sub-arc (~95 km) mantle conditions (Syracuse et al., 2010). Reverse heating experiments involve heating the sample to a high-T and slowly cooling it to the target temperature. This method helps to produce large crystals for robust microprobe analyses. To check that the reverse experiment does not form high-T minerals in disequilibrium with low-T mineral assemblages, we performed a forward heating experiment (where the experiment was only heated to the target T) at 900 °C and 2 GPa and compared the phase equilibria between the forward and reverse heating experiments. Energy dispersive spectroscopy (EDS) analyses and backscattered electron (BSE) imaging were done at the Geo Arizona SEM Laboratory, University of Arizona. The major and minor oxide analyses of the melts and minerals were done using CAMECA SX100 electron microprobe (EMPA) at Kuiper-Arizona Laboratory for Astromaterials Analysis at the University of Arizona. The phase proportions (wt.%) and the bulk residual compositions were calculated via mass balance using the *Excel Solver* analysis tool. pMELTS thermodynamic software, which is optimized to explore 'mantle-like' bulk compositions at fore-arc to sub-arc conditions (1000–2000 °C and 1–3 GPa; Ghiorso et al., 2002), was run using the bulk compositions and P-T conditions of this study to test whether it can reproduce the phase equilibria in our experiments. More details of the starting material synthesis, experimental procedure, EDS and EMPA operating conditions, mass balance calculations and pMELTS inputs can be found in Supplementary Information, S1.

3. Results

3.1. Approach to equilibrium

The assessment of equilibrium in the experiments were determined based on: (a) low values of the sum of residual squares ($\sum r^2 < 1$) during mass balance even when adding a pure aqueous fluid to the system (Table S3); (b) lack of substantial chemical heterogeneity in the mineral phases (Fig. 1 and 2); (c) Kd_{Melt}^{Ol} (Fe-Mg) range between 0.20 to 0.36 at 2 GPa and 0.35 at 3 GPa (Table S3) which is within the range of previous studies (e.g., Mallik et al., 2016); (d) the presence of triple junction among grain boundaries (Fig. 1). See Supplementary Information, S1 for further details.

3.2. Texture and phase equilibria

Forward heating experiments that involve heating the sample straight to the targe temperature show similar mineral phase equilibria, mineral abundance (wt.%), and composition, as well as similar texture in the system (See Table 1, sample 66B and 112B; Figure S2, x). The crystal sizes were significantly smaller in the forward experiment.

Table 2

At 2 GPa (~65 km depth) and at $T < 1050$ °C the samples consist of olivine and orthopyroxene distributed throughout the inner capsule and mica, amphibole and oxides (magnetite-spinel mixture) are usually located near the bottom (Fig. 1). These samples show high porosity at the grain boundaries and at the top of the capsule, which are filled by Si-rich quench spheres and wisps - quench textures that indicate the saturation of fluids in the system (Till et al., 2012). Upon increasing the pressure to 3 GPa (~95 km depth) and at $T < 1100$ °C, the samples show a similar texture with olivine and orthopyroxene throughout the capsule and garnet and mica form near the bottom (Fig. 1). A layer of large olivine grains forms between the orthopyroxene assemblage (± garnet ± oxide) and the quench melt pools that appear near the top of the capsule ($T > 1100$ °C at 2 and 3 GPa). These melt pools consist of heterogeneous quench matter with acicular and dendritic grains forming "fan-like" shapes.

Pressure has an important role in: (1) The mineral stability of low-density (e.g., chlorite, mica, amphibole) and high-density minerals (e.g., oxides, garnet, spinel)- At fore-arc depths (~65 km) serpentine-rich matrices dehydrate and transform into olivine-orthopyroxenites with minor abundances of mica and amphibole (~1–7 wt.%) and oxides (<2 wt.%), and at greater depths (~95 km) they transform into a denser garnet-peridotite (1–9 wt.% garnet) that can contain oxides (~2 wt.%). (2) The primary magma composition- Melting these lithologies produces basaltic primary magmas although the magmas produced at deep fore-arc depths (~65 km) are rich in SiO_2, FeO, alkalis and TiO_2, and slightly depleted in Ca and MgO (~52 wt.% SiO_2, ~12 wt.% FeO, ~2.6 wt.% alkalis, ~0.6 wt.% TiO_2, ~3 wt.% CaO, ~11 wt.% MgO) than the magmas derived at ~95 km (~46 wt.% SiO_2,~11 wt.% FeO, ~2 wt.% alkalis, ~0.35 wt.% TiO_2, ~5 wt.% CaO, ~17 wt.% MgO) (Figure S6). (3) The location of the inferred solidus- The increase of pressure from 2 to 3 GPa increases the solidus T by ~25 °C (discussion in the next section). (4) The increase of pressure decreases the melt productivity by 1–5% at similar temperatures (Fig 2).

Temperature also has an important effect on: (1) The stability of hydrous minerals (e.g., chlorite, mica, amphibole) - At ~65 km depth (2 GPa), chlorite is stable up to ~800 °C and mica and amphibole up to ~1050 °C. These hydrous minerals together with olivine and oxide are eventually consumed to produce abundant orthopyroxene (ol/opx =~0.3), oxide, and aqueous fluids. Above the inferred solidus (>1050 °C), orthopyroxene and oxides are consumed (ol/opx =~1.4) to produce olivine and melt (Supplementary Information S5, ii and vi). The oxides are stable up to ~1150 °C. At ~95 km depth and below the inferred solidus, garnet and oxides are stable. Orthopyroxene is dominant (ol/opx=0.3) but is eventually consumed (ol/opx=1) together with garnet and oxides to produce melt (Supplementary Information S4, viii and ix). (2) The melt composition: The low-degree melts are rich in Al_2O_3 (~17 wt.%) and CaO (~3 wt.%) and their contents decrease as the T increases and the overall Mg# increases from ~64 to ~76. (3) The melt productivity - melt productivity increases with increasing T but decreases at $T >$ 1200 °C because some melt and residual aqueous fluids are consumed to produce olivine and orthopyroxene (Supplementary Information S4, iv-vii).

The increase of water contents from 5 to 10 wt.% seems to influence (1) The phase equilibria stability and their abundance - At ~65 km, the bulk proportion of hydrous minerals decreases from ~7 wt.% to ~3 wt.% and the oxides decreases from >2.6 wt.% to <1 wt.%, as the bulk H_2O in the system increases from 5 to 10 wt.% H_2O (Figure S7). (2) Melt productivity - water saturated systems (5–10 wt.% H_2O) show a similar melting behavior but diverge at $T \geq 1200$ °C (Fig. 2). At 5 wt.% bulk H_2O and below the solidus (<1050 °C), olivine, amphibole, mica, and chlorite are consumed to produce orthopyroxene, oxides, and fluids (Supplementary Information S4, i). Above the inferred solidus (>1050 °C), abundant orthopyroxene and minor olivine, oxides, and fluids are consumed to produce exponential melt productivity until ~1200 °C (Eq. 1; Supplementary Information S4, ii), when the proportion of aqueous fluids decreases from ~4.5 to ~1 wt.%. From 1200 °C to 1225 °C the melt productivity decreases (Eq. (2)) because most of the aqueous fluids almost dissolve in the melt and orthopyroxene is the only reactant phase to produce olivine and melt (Supplementary Information S4, iii). From 1225–1250 °C the aqueous fluids and melt are consumed (Eq. (3)) to produce olivine and orthopyroxene (Supplementary Information S4, iv).

Upon adding 10 wt.% H_2O to the system, the melt productivity increases exponentially up to ~1225 °C (Fig. 2) due to the increased stability of a distinct aqueous fluid phase that leads to an overall enhancement of melt productivity. From 1225 to 1250 °C, the melt productivity is reduced (Eq. (4)) because aqueous fluids and melt are consumed to produce olivine and orthopyroxene (Supplementary Information S4, vii).

$$F(\%)_{\ 1150\ to\ 1200^{\circ}\mathrm{C}} = \left(3 \times 10^{-8}\right)e^{0.0170T}\ \left(\mathrm{R}^2 = 0.989\right) \tag{1}$$

$$F(\%)_{\ 1200\ to\ 1225^{\circ}\mathrm{C}} = 0.0911T - 83.01\ \left(\mathrm{R}^2 = 1\right) \tag{2}$$

$$F(\%)_{\ 1225\ to\ 1250^{\circ}\mathrm{C}} = -0.2081T - 283.47\ \left(\mathrm{R}^2 = 1\right) \tag{3}$$

$$F(\%)_{\ 1225\ to\ 1250^{\circ}\mathrm{C}} = -0.2193T - 310.69\ \left(\mathrm{R}^2 = 1\right) \tag{4}$$

At ~95 km (3 GPa) and at 10 wt.% H_2O in the system, the melt productivity increases exponentially up to ~1200 °C (*Eq. (5)*) by melting orthopyroxene, garnet, and oxides (Supplementary Information S4, viii). However, it decreases towards ~1250 °C (*Eq. (6)*) where orthopyroxene is consumed to produce olivine and melt (Supplementary Information S4, iv).

$$F(\%)_{\ 1150\ to\ 1200^{\circ}\mathrm{C}} = \left(2 \times 10^{-13}\right)e^{0.0271T}\ \left(\mathrm{R}^2 = 1\right) \tag{5}$$

$$F(\%)_{\ >1200^{\circ}\mathrm{C}} = 0.0306T - 8.041\ \left(\mathrm{R}^2 = 1\right) \tag{6}$$

These melt productivity relations above (Eq. (1)-4) can be used by future geodynamic studies to predict melting degrees in subduction zones due to serpentine-rich mélanges.

4. Discussion

4.1. The inferred wet solidus of serpentine-rich matrices from 2 to 3 GPa

The wet solidus of hydrous serpentinite-rich mélanges (5–10 wt.% H_2O) at 2 GPa (~65 km) is determined by the following: (1) Breakdown of mica and amphibole between 1050 – 1100 °C (Table S4), contributing to melt production. (2) Abrupt change in Ol/Opx ratio - at $T < 1050$ °C,

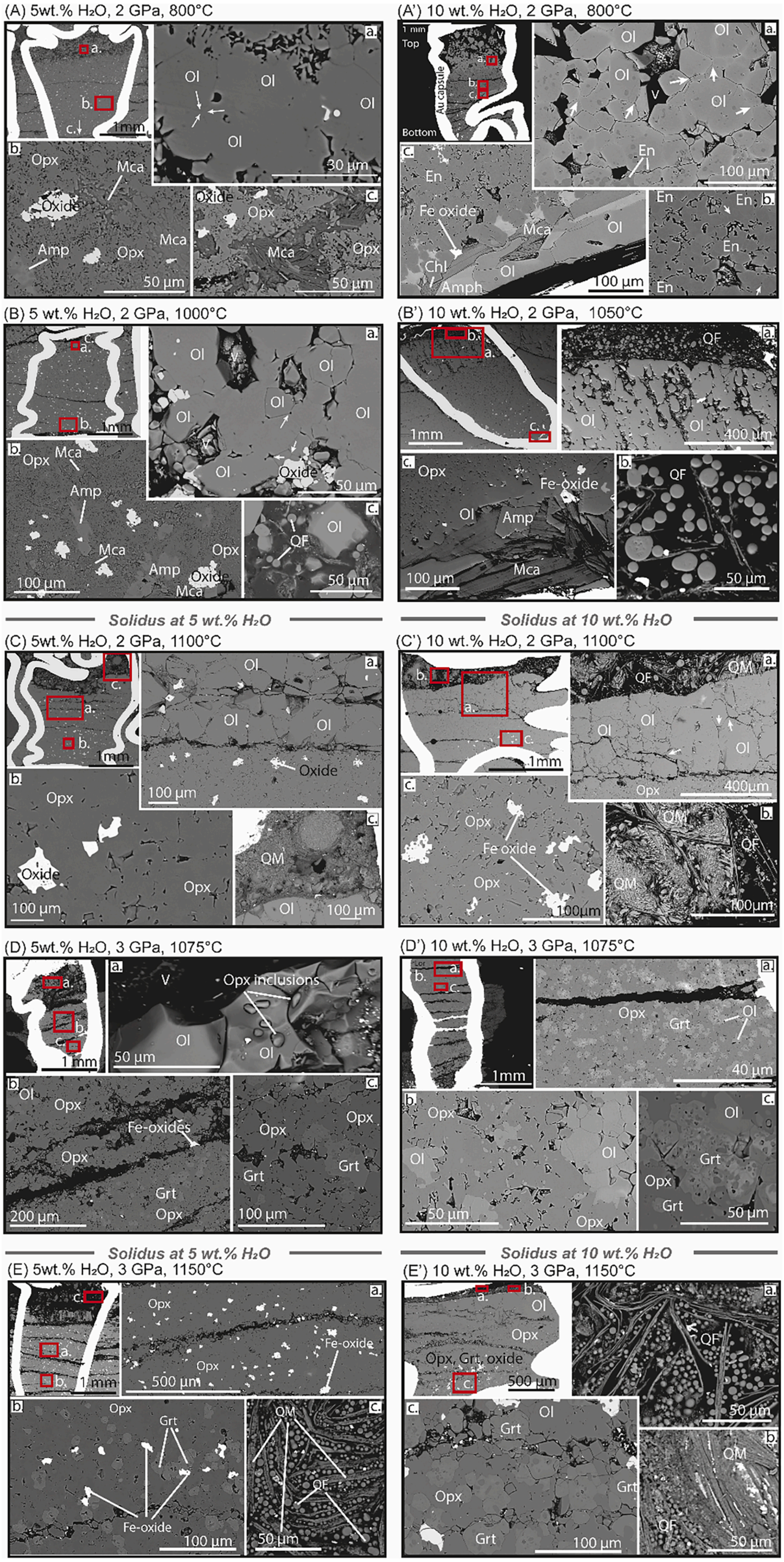

Fig. 1. Representative backscattered electron (BSE) images for the set of experiments at 2 GPa, under and above the solidus for 5 wt.% H_2O (A, B,C) and 10 wt.% H_2O (A', B',C'). White arrows indicate triple junctions. Representative backscattered electron (BSE) images for the set of experiments at 3 GPa, under and above the solidus for 5 wt.% H_2O (D, E) and 10 wt.% H_2O (D', E'). The inferred solidus location is indicated with a grey solid line.

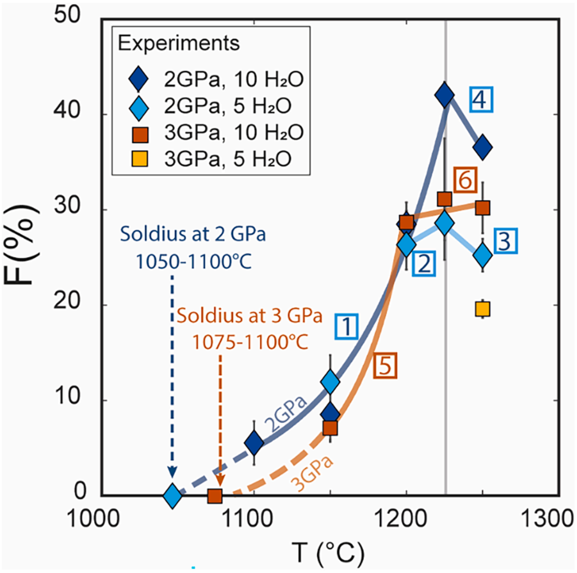

Fig. 2. Melt fraction (%) as a function of *T*. The inferred solidus of serpentine-rich matrices at 2–3 GPa (~65–95 km) for both water content in the system is indicated with blue and orange arrows. The number in a square indicates the equation number in the main text. The gray vertical line indicates when the melting decreases at $T > 1225$ °C due to melt consumption and more olivine and orthopyroxene precipitation. The error bars are smaller than the symbol sizes for specific data points.

orthopyroxene is predominant (ol/opx =0.3) and at $T > 1100$ °C, orthopyroxene is consumed to produce olivine (ol/opx >1) and melt (Table S4), indicating that likely the onset of partial melting occurred between 1050 – 1100 °C. (3) Mg# change in the mineral phase composition and MgO, Al_2O_3 and CaO content variation in orthopyroxene (Figure S8) which is interpreted to be the result of mineral-melt partitioning (e.g., Till *et al.,* 2012; Lakey and Hermann, 2022). (4) The water/fluid phase abundance (wt.%), coexisting with mica and amphibole, remains nearly constant until it decreases at ~1050–1100 °C with the presence of hydrous melts (Figure S8). (5) Increase of porous texture in excess fluid-mediated conditions ($T \leq 1050$ °C) compared to low porosities in melt-mediated conditions ($T > 1100$ °C) (Fig. 1). (6) Difference in olivine grain growth under fluid-mediated (≤100 μm at $T \leq$ 1050 °C) versus melt-mediated (≥200 μm at $T > 1100$ °C) conditions, where the grains are larger and euhedral in the latter (Fig. 1). All these observations indicate that the solidus of serpentine-rich matrices at 2 GPa (~65 km) must be located between 1050 °C and 1100 °C. The same approach has been used to infer the solidus *T* at 3 GPa (~95 km) that is located between 1075 and 1100 °C. Therefore, serpentine-rich matrices have a narrow solidus *T* between ~1050–1100 °C from ~65 to 95 km depth.

4.2. Limitations of pMELTS modeling using serpentine-rich mélange compositions

Although pMELTS thermodynamic software is optimized to explore ‘mantle-like’ bulk compositions at sub-arc conditions (1000–2000 °C and 1–3 GPa; Ghiorso et al., 2002), we observe that it has some limitations for serpentine-rich mélange-like systems. The melting curves predicted by pMELTS at 2 GPa follow a similar topology to the experimental curve up to 1225 °C but are shifted to lower temperatures (~50 °C). However, at 3 GPa, it predicts significantly lower melt fractions compared to the experimental data at similar temperatures. For example, at 1200 °C pMELTS predicts $F < 5\%$ whereas the experiments show $F > 25\%$. The difference in melt production is attributed to the difference in mineral stabilities between the modeling and the experiments. The mineral stability predicted by the software also affects the chemistry of the melts by under or over-predicting the major element contents (Figure S9). Therefore, we conclude that, at least for serpentine-rich bulk compositions, the software can fairly predict phase equilibria (including the detection of a water phase) at 2 GPa but is not well-suited at ≥3 GPa. The melting curve equations predicted by pMELTS can be found in Supplementary Information S5, and the pMELTS inputs and outputs can be found at the University of Arizona *Re*DATA (doi: 10.25422/azu.data.26132167).

4.3. Assessing the formation of diapirs from forearc to subarc depths

Diapiric rise of mélanges has been proposed as an effective mass-transfer mechanism from the slab to the overriding lithosphere in subduction zones (e.g., Castro et al., 2010; Marschall and Schumacher, 2012; Nielsen and Marschall, 2017; Codillo et al., 2023). However, to assess whether diapirism can occur for ultramafic mélanges during subduction, three key parameters need to be considered at the appropriate *P-T* conditions: (1) Positive buoyancy or density contrast between the mélange and the overlying mantle-wedge, (2) bulk viscosity, i.e., the viscosities of the mélange and the mantle-wedge, and (3) thickness of the mélange. With these three parameters, the dominant (i.e., fastest) timescale of diapir growth can be calculated using the following relation from Turcotte and Schubert (2014):

$$\tau_a = \frac{13.04\mu}{(\Delta\rho)gb} \tag{7}$$

where μ represents an isoviscous system where the mantle and the mélange have similar viscosity (explained in detailed below), $\Delta\rho$ is the density difference between the mantle wedge and solid mineral assemblage in the mélange matrix, g is gravitational acceleration, b is the thickness of the mélange, and τ_a is the fastest or the dominant timescale for instability formation.

Here, we calculate the residual mineral density of serpentine-rich mélange during dehydration and melting by using the phase modes (wt.%) and mineral phase compositions from the experiments in this study (Supplementary Information S3, Table S12). The densities from the experiments feed into the buoyancy assessment in Eq. (7), as discussed below. It is essential to clarify that $\Delta\rho$ reflects the density of the ultramafic-rich mélange matrix with minor sedimentary components or can also reflect the density of an ultramafic mélange matrix with minor metasedimentary blocks. For a mélange that contains more HP mafic blocks (e.g., eclogite, amphibolite, greenschist, blueschist), the densities may be even higher. Fig. 3 shows the density contrast for serpentine-rich mélanges (this study) and for chlorite-rich mélanges from previous studies as a function of *T*. Serpentine-rich mélanges are not likely to form diapirs because they densify relative to the overlying mantle wedge during dehydration at $T \geq 800$ °C and remain stable in the subduction channel. The buoyancy of chlorite-rich mélanges is mainly controlled by their composition, where metaluminous bulk mélanges can be more buoyant down to deep forearc depths than peraluminous bulk mélanges because the latter form abundant garnet at shallower depths (Lakey and Hermann, 2022; Codillo et al., 2023). Fig. 3 shows that all chlorite-rich mélanges will lose their positive buoyancy at ≥1000 °C due to their transformation to denser lithologies containing orthopyroxene, olivine, spinel/oxides (± garnet). Thus, even if a chlorite-rich mélange diapir initiates from the slab top, it would effectively stall once it ascends and thermally equilibrates with the hotter mantle wedge (>1000 °C).

Given the dearth of experimentally determined flow laws specific to these ultramafic-rich mélanges at the desired *P-T* conditions, we assumed reasonable viscosity ranges that could be used to assess the feasibility of diapirism. The viscosity of the mantle wedge, from forearc to sub-arc depths, can vary between 10^{21} Pa·s to as low as 10^{18} Pa·s due to the influx of fluids from the subducting slab (Hirth and Kohlstedt, 2003). If the viscosity of the mantle is at the very high-end (e.g., $>10^{20}$ Pa·s), ascent of diapirs will likely be inhibited. Therefore, we consider

Table 1
Starting material (S.M.) composition (wt.%) used in this study and experimental conditions and run products at 2 and 3 GPa.

Oxides	SiO_2	TiO_2	Al_2O_3	Cr_2O_3	FeO	MnO	MgO	CaO	Na_2O	K_2O	P_2O_5	Mg#									
S.M.	48.93	0.08	4.02	0.01	10.58	0.17	35.39	0.31	0.32	0.18	0.01	86									
Sample	P	T	H_2O	Ol	±σ	Opx	±σ	Amp	±σ	Mca	±σ	Grt	±σ	Chl	±σ	Oxide	±σ	Melt	±σ	Fl	±σ
14B_a	2	800	10	22.4	1.1	65.9	2.9	1.2	1.7	0.3	0.4	–		0.3	0.46	–		–		9.9	0.1
66B[*]	2	900	10	23.8	0.2	61.7	2.4	1.5	1.0	1.7	1.5	–		–		1.4	0.3	–		9.8	0.2
112B	2	900	10	23.9	0.1	64.4	0.43	+		+		–		–		1.6	0.1	–		10.0	0
65B	2	1000	10	24.3	0.4	60.9	1.6	1.4	1.2	2.4	1.7	–		–		1.0	0.3	–		9.9	0.1
93B	2	1050	10	21.6	0.2	67.2	0.8	0.2	0.3	0.2	0.3	–		–		0.8	0.3	–		10.0	0.0
1B	2	1100	9	27.0	1.6	58.7	3.0	–		–		–		–		0.4	0.0	5.5	2.3	8.4	0.9
15A	2	1150	9	26.5	1.8	56.5	3.5	–		–		–		–		0.6	0.1	8.5	2.9	7.9	1.1
7A	2	1200	9	34.4	1.8	33.1	2.5	–		–		–		–		–		28.5	2.3	4.1	1.6
9A	2	1225	9	33.2	1.1	23.0	1.6	–		–		–		–		–		42.0	1.4	1.7	1.6
94B	2	1250	10	34.5	0.8	27.9	1.0	–		–		–		–		–		36.6	1.0	1.0	1.1
62B	2	800	5	19.9	0.9	65.7	1.0	3.2	0.7	1.9	1.3	–		2.1	1.69	2.6	0.0	–		4.6	0.1
52B	2	900	5	28.9	0.7	59.9	3.5	–		6.9	3.5	–		–		+		–		4.4	0.5
59B	2	1000	5	19.4	0.3	70.2	2.7	0.8	1.1	1.5	1.3	–		–		3.2	0.1	–		5.0	0.0
71A	2	1100	5	23.9	0.3	68.7	0.7	–		–		–		–		2.3	0.5	+		5.1	0.0
68A	2	1150	5	25.9	2.2	57.8	3.5	–		–		–		–		2.7	0.0	11.9	2.8	1.7	1.5
53B	2	1200	5	25.6	1.0	47.2	2.8	–		–		–		–		–		26.3	2.6	0.9	1.2
58B	2	1225	5	28.2	1.4	41.6	1.9	–		–		–		–		–		28.6	1.8	1.6	1.5
92B	2	1250	5	31.0	0.8	43.0	1.8	–		–		–		–		–		25.2	1.7	0.8	1.2
69B	3	1000	10	16.2	0.5	65.9	1.2	–		–		1.8	2.1	–		6.1	1.5	–		10.0	0.1
97A	3	1075	10	31.0	0.5	49.2	2.4	–		–		9.7	2.0	–		+		–		10.0	0.0
12B	3	1150	10	25.9	0.8	54.0	1.5	–		–		4.4	0.9	–		1.0	0.0	7.1	0.7	7.6	0.8
95B	3	1200	10	27.3	1.6	43.7	0.9	–		–		–		–		–		28.7	2.0	0.3	0.5
99B	3	1225	10	28.6	5.3	36.1	3.7	–		–		–		–		–		31.1	3.7	4.2	4.1
98A	3	1250	10	34.0	2.5	33.6	3.2	–		–		–		–		–		30.2	2.9	2.2	2.2
82A	3	1000	5	22.0	1.5	65.6	5.1	–		–		4.7	3.5	–		2.7	0.1	–		5.0	0.0
97A	3	1075	5	32.4	0.6	52.3	1.1	–		–		10.3	0.5	–		–		–		5.0	0.0
83B	3	1150	5	23.2	0.1	62.4	1.8	–		–		7.3	1.4	–		2.0	0.3	+		5.0	0.0
102A	3	1250	5	28.8	0.4	44.8	1.4	–		–		6.8	3.1	–		–		19.6	4.1	–	0.0

[*] Sample 66B is the reversed experiment, and Sample 112B is the forward experiment at the same run conditions. The plus sign (+) denotes the trace presence of the mineral phase (observable), but not detected by mass balance. The minus sign (–) denotes the absence of the mineral from the system. Pressure (P) is in GPa, Temperature (T) is in °C, and water content in the system (H_2O) is in wt.%. The sigma (±σ) indicates standard deviation as ±1σ obtained from several microprobe analyses. Abbreviations: Ol, olivine; Opx, orthopyroxene; Am, amphibole; Mca, mica; Chl, chlorite; Grt, garnet; oxide, magnetite-spinel mixture; Fl, aqueous fluid.

Table 2
Composition of the anhydrous experimental melts (wt.%).

Sample	P	T	H_2O		SiO_2	TiO_2	Al_2O_3	Cr_2O_3	FeO	MnO	MgO	CaO	Na_2O	K_2O	P_2O_5	Mg#
1B	2	1100	9	$n = 4$ *	51.5	0.6	17.9	0.0	11.7	0.2	11.6	3.1	2.0	1.1	0.3	64
				±σ	2.3	0.0	0.3	0.0	0.3	0.0	1.7	0.3	0.1	0.2	0.0	16
15A	2	1150	9	$n = 3$	52.3	0.5	16.9	0.0	12.7	0.3	11.3	3.3	1.8	0.6	0.3	61
				±σ	0.6	0.0	0.7	0.0	0.2	0.0	1.2	0.1	0.2	0.1	0.1	12
7A	2	1200	9	$n = 7$	51.3	0.3	13.3	0.0	13.4	0.2	17.8	1.9	0.8	0.7	0.3	70
				±σ	1.7	0.0	0.0	0.0	0.0	0.0	0.9	0.2	0.3	0.3	0.1	6
9A	2	1225	9	$n = 8$	52.0	0.2	10.8	0.0	12.3	0.2	21.7	1.6	0.6	0.4	0.1	76
				±σ	1.0	0.0	0.1	0.0	0.2	0.0	1.0	0.0	0.1	0.0	0.0	5
94B	2	1250	10	$n = 5$	51.2	0.0	11.4	0.0	14.9	0.2	19.6	1.7	0.5	0.2	0.2	70
				±σ	0.8	0.0	0.1	0.0	0.4	0.0	1.1	0.1	0.0	0.1	0.0	7
68A	2	1150	5	$n = 5$	53.5	0.5	15.8	0.0	11.8	0.2	13.2	2.4	1.3	0.9	0.3	67
				±σ	0.8	0.0	0.4	0.0	0.3	0.0	0.6	0.0	0.2	0.0	0.0	5
53B	2	1200	5	$n = 8$	48.4	0.3	13.4	0.0	12.0	0.1	22.4	2.3	0.7	0.3	0.1	77
				±σ	1.2	0.0	0.4	0.0	0.1	0.0	1.0	0.1	0.2	0.1	0.0	6
58B	2	1225	5	$n = 4$	47.7	0.3	13.6	0.0	16.7	0.2	19.7	0.8	0.4	0.4	0.1	68
				±σ	2.3	0.0	1.2	0.0	0.1	0.0	0.4	0.2	0.1	0.2	0.0	2
92B	2	1250	5	$n = 5$	49.1	0.0	12.8	0.0	17.2	0.2	17.6	2.2	0.5	0.1	0.2	65
				±σ	1.2	0.0	0.6	0.0	1.5	0.0	0.1	0.2	0.1	0.0	0.0	4
12B	3	1150	10	$n = 3$	46.8	0.4	16.5	0.0	11.1	0.2	17.8	5.1	1.4	0.7	0.1	74
				±σ	1.2	0.0	1.5	0.0	0.8	0.0	4.3	0.8	0.5	0.3	0.0	
95B	3	1200	10	$n = 4$	49.2	0.0	13.9	0.0	11.0	0.1	22.5	2.5	0.1	0.6	0.1	78
				±σ	1.2	0.0	1.5	0.0	0.8	0.0	4.3	0.8	0.5	0.3	0.0	
99B	3	1225	10	$n = 5$	50.5	0.0	12.5	0.0	13.2	0.2	21.7	1.2	0.4	0.2	0.1	74
				±σ	6.4	0.0	1.5	0.0	1.1	0.0	5.7	0.5	0.3	0.2	0.0	31
98A	3	1250	10	$n = 6$	52.7	0.0	12.5	0.0	11.4	0.2	20.0	2.3	0.5	0.3	0.1	76
				±σ	2.7	0.0	0.2	0.0	1.2	0.0	0.8	0.0	0.2	0.3	0.1	6
102A	3	1250	5	$n = 6$	50.3	0.0	12.0	0.0	12.4	0.2	21.2	3.0	0.7	0.1	0.2	75
				±σ	0.9	0.0	0.0	0.0	0.7	0.0	0.1	0.0	0.2	0.0	0.1	6

[*] n, indicates the number of analyses. Pressure (P) is in GPa, Temperature (T) is in °C, and water content in the system (H_2O) is in wt.%. The sigma (±σ) indicates standard deviation as ±1σ obtained from several microprobe analyses. Mg# =[molar ratio of MgO/(MgO+ molar FeO].

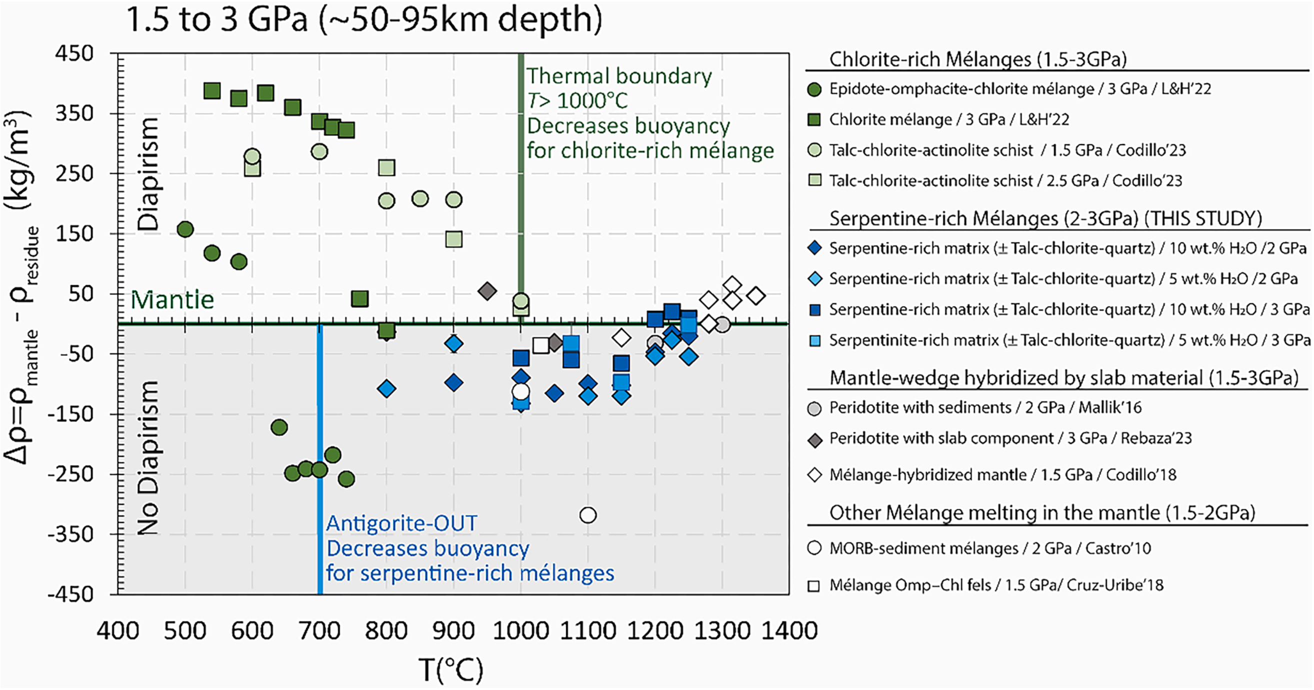

Fig. 3. Density contrasts of ultramafic-rich lithologies relative to the peridotite mantle ($\Delta\rho=\rho_{\text{matle}}\ _{-}\rho_{\text{lithology}}$) at P-T conditions. The density of the lithologies at $P \leq 2.5$ GPa was compared to that of a spinel-lherzolite (Xu, 2000), whereas at 3 GPa were compared to that of a garnet-lherzolite (Davis et al., 2011) at the same P-T conditions (See Table S12). The legend refers to the type of ultramafic-rich rock used in literature and this study. Above the Δρ=0 line (positive values), the lithology is lighter, and diapirism may occur. Under the Δρ=0 line (negative values), the lithologies are denser and remain stable at the slab-mantle interface (no diapirism). For subducted chlorite mélanges, the density contrasts of epidote-omphacite-chlorite mélanges and chlorite mélanges are calculated using the densities provided by Lakey & Hermann (2022). The density contrasts of tremolite-chlorite schists and talc-chlorite-actinolite schists are calculated using the densities reported by Codillo et al. (2023). For reference, the density of peridotite hybridized by slab material (Mallik et al., 2016; Rebaza et al., 2023) and other mélange melting (Castro et al., 2010; Cruz-Uribe et al., 2018) are also included. The green vertical line indicates the potential thermal boundary (≥1000 °C) where chlorite-rich mélanges lose buoyancy. The blue vertical line indicates antigorite breakdown at $T > 700$ °C, indicating that serpentine-rich mélanges may lose buoyancy above that temperature. The error bars from this study are smaller than the symbol sizes.

the lower range of mantle viscosities (e.g. 10^{18} to 10^{19} Pa·s) which may be favorable for diapirism. From field observations, serpentine-rich matrices have similar viscosities, between 10^{18} and 10^{19} Pa·s (Grigull et al., 2012). Given the order of magnitude uncertainty in matrix viscosities, the effect of blocks in composite block-matrix viscosities is expected to be encapsulated within that range (Grigull et al., 2012). Therefore, we explored an isoviscous system with viscosities varying from 10^{18} to 10^{19} Pa·s. The thickness range of the mélange is assumed to be the same as that of the subduction channel which ranges from hundred meters to ~8 km, as inferred by field and geophysical observations (Abers, 2005; Zhang, 2020; and references therein). To assess the feasibility of instability formation in the mélanges, we adopt a similar approach to that of Ho et al. (2019) where they discuss the importance of slab subduction timescales (τ_s) to allow the formation and growth of instabilities (τ_a):

$$\tau_s = \frac{\frac{h}{\sin(\theta)}}{V_s} \tag{8}$$

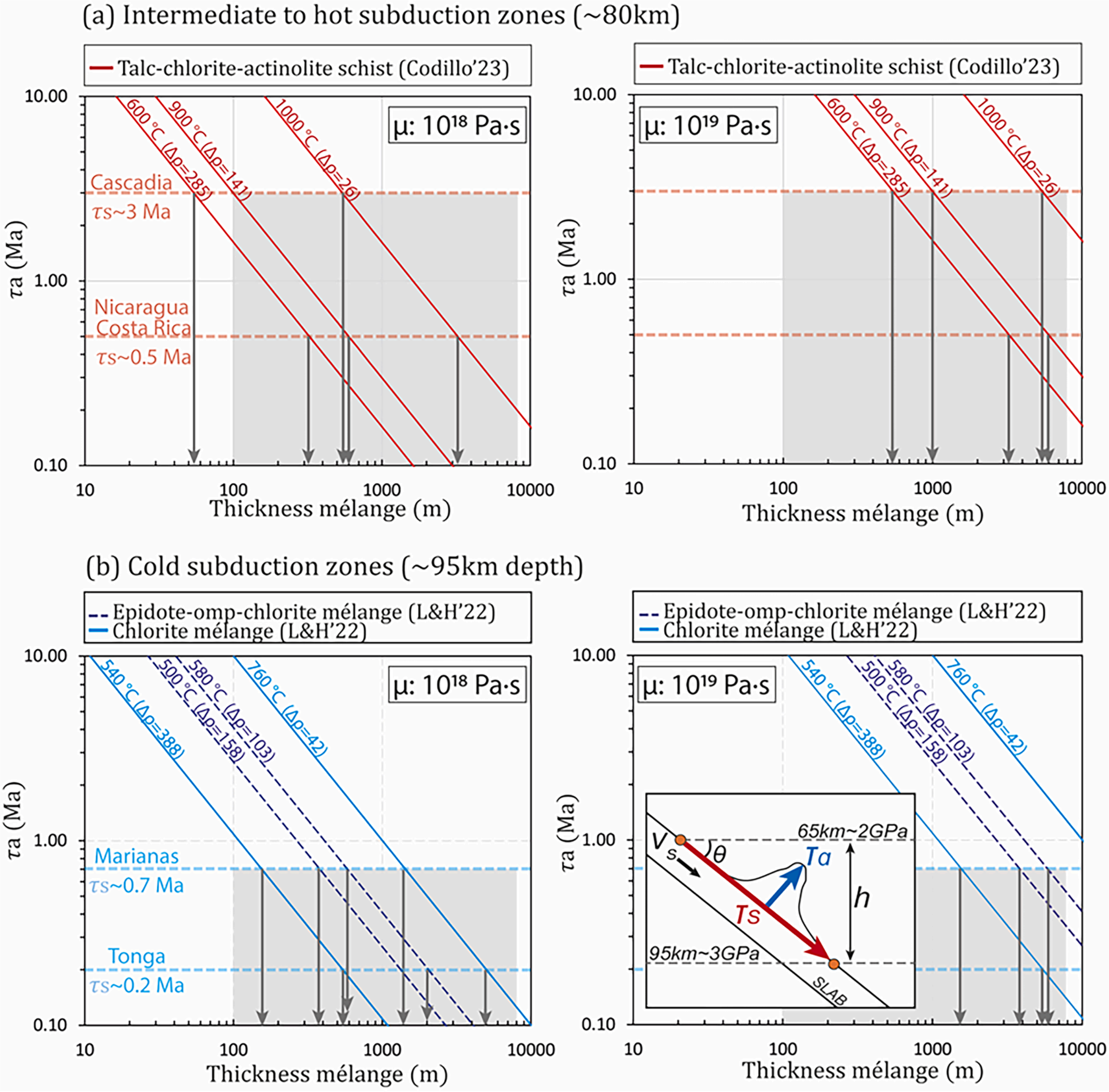

Fig. 4. Shortest instability growth timescales (Ma) vs. thickness of chlorite-rich mélanges in (a) hot and (b) cold subduction zones. The solid curves are the timescales for diapir growth and include the viscosity of the system (μ), density contrast (Δρ), and thickness (*b*), as shown in Eq. (7). Note that the pressure and temperature effects are already included in the bulk density (mineral phase transformation). Sub-figure (a) shows the shortest instability growth timescales for talc-chlorite-actinolite schist (Codillo et al., 2023) at 2.5 GPa from 600 to 1000 °C. The horizontal red dashed lines indicate the time of slab subduction (τ_s) from ~65 km to ~95 km depth (~2 to 3 GPa) for the hottest slab subduction geotherms (Cascadia and Nicaragua/Costa Rica). Figure (b) shows the shortest time instability growth for epidote-omphacite-chlorite and chlorite mélanges (Lakey and Hermann, 2022) at 3 GPa and from 500 to 760 °C. The horizontal blue dashed lines indicate the time of slab subduction (τ_s) for the coolest slab subduction geotherms (Marianas and Tonga). In all the sub-figures, the gray-shaded area indicates the subduction channel thickness range inferred by field and geophysical observations (Zhang, 2020; and references therein). The downward gray arrows indicate the minimum required thickness of the mélange to form an instability. The sketch in the inset of the bottom left sub-figure represents Eq. (8) in the main text.

where h is the distance between two points in the subduction channel (km), and in this case, it is 30 km (i.e., between the depths of 65 to 95 km), θ is the slab dip (°), and V_s is the slab velocity (km/Ma) retrieved from Syracuse *et al.* (2010). Accordingly hot slab subduction zones such as Central Cascadia would take ~3 Ma to subduct from ~65 to 95 km depth, and Nicaragua and Costa Rica would take ~0.5 Ma. Cold slab subduction timescales are generally faster, with ~0.2 Ma for Tonga and ~0.5 Ma for Marianas (Table S13).

Fig. 4 shows the interplay of mélange density, viscosity, thickness, and the slab subduction timescales on diapir growth timescales. In a hot subduction zone at depths of ~80 km (Fig. 4a), viscosity of 10^{18} Pa·s, and the timescales of subduction as ~0.5–3Ma, the talc-chlorite-actinolite mélange channel at 600 °C ($\Delta\rho$ =285) requires a thickness of ~55 to 300 m to become buoyant (note that 55 m is below the indicated thickness range in grey shade). At 900 °C ($\Delta\rho$ =141), the density contrast decreases due to the formation of pyroxenes and requires a ~100 to ~600 m thickness. Increasing the temperature to ~1000 °C ($\Delta\rho$ =26), the chlorite-rich mélange requires ~550 m to ~3 km thickness to form instabilities. We want to emphasize that the slowest hot slabs (e.g., Cascadia) require thinner mélange thicknesses compared to relatively faster hot subduction (e.g., Nicaragua and Costa Rica). This is because the slab with the slowest subduction timescales allows sufficient time to form instabilities compared to fast subduction timescales. On the other hand, cold subduction zones (Fig. 4b) subduct material much faster (~0.2–0.7 Ma) and at similar viscosities (10^{18} Pa·s) require greater thicknesses despite their lower bulk density. For example, at ~95 km depth and 540 °C ($\Delta\rho$ =388), the required thickness for a chlorite-rich mélange must be ~160 to ~550 m to form instabilities. At 760 °C ($\Delta\rho$ =42), the mélange densifies and requires a larger thickness of ~1.5 to ~5 km. For an epidote-omphacite-chlorite mélange at 500 °C ($\Delta\rho$ =158) requires ~380 m to ~1.5 km thickness and by increasing the temperature to 580 °C ($\Delta\rho$ =103), the thickness increases from ~580 m to ~2 km to initiate instabilities.

Given that viscosity scales linearly with τ_a (Eq. (7)), the increase of viscosity from 10^{18} to 10^{19} Pa·s would imply that the minimum required mélange thickness to form the fastest diapir increases by one order of magnitude as well. For example, in hot subduction zones (Fig. 4a), under the same conditions as before and only increasing the viscosity to 10^{19} Pa·s, the required thickness range for a talc-chlorite-actinolite mélange at 600 °C ($\Delta\rho$ =285) increases by an order of magnitude to ~550 m to ~3 km (compared to 55 m to 300 m, when the viscosity was 10^{18} Pa·s). Similarly, at 900 °C ($\Delta\rho$=141) increases to ~1 km to ~6 km, and at 1000 °C ($\Delta\rho$ =26) increases to ~5.5 km to ~30 km (where, 30 km is beyond the thickness range in gray, Fig. 4a). For cold subduction zones (Fig. 4b), the viscosity increase to 10^{19} Pa·s also increases the required mélange thicknesses by one order of magnitude. For example, chlorite-rich mélanges at 540 °C ($\Delta\rho$=388) require thicknesses increases to ~1.6 to ~5.5 km to form a diapir, and at 760 °C ($\Delta\rho$ =42) increases to ~20 to ~60 km. An epidote-omphacite-chlorite-rich mélange at 500 °C ($\Delta\rho$ =158) would require ~3.8 to ~15 km thickness, and at 580 °C ($\Delta\rho$ =103) increases to ~5.8 to ~20 km of thickness. Thus, under certain conditions the required thicknesses are beyond the observed range, rendering diapirism ineffective.

The above discussion suggests that fast and cold subduction channels (e.g., Tonga and Marianas) require thicker mélanges and under certain conditions, the required thicknesses can be beyond the observed range in nature. Thus, the formation of ultramafic-rich mélange diapirs (serpentine and chlorite-rich) in cold channels may not be as feasible as previously thought (e.g., Marschall and Schumacher, 2012; Codillo et al., 2023). In hot subduction zones, mélanges dehydrate and densify. However, slower, hot subduction channels (e.g., Cascadia) are more likely to form diapirs since they require a thinner mélange thickness mostly within the observed thickness range. It is crucial to emphasize that any buoyant diapir in cold or hot subduction zones can potentially stall as they approach the thermal boundaries at $T \geq 800$ °C for serpentine-rich mélanges and at $T \geq 1000$ °C for chlorite-rich mélanges (Fig. 4). However, we cannot completely rule out the presence of diapirs in sediment-starved subduction zones. One way for ultramafic-rich mélanges to retain their positive buoyancy in the mantle wedge would be if the ascent timescales are faster than the timescales required to thermally equilibrate the entire diapir from its core to the rim which requires further assessment in a future study. In summary, our study provides a framework that future studies may use to assess the feasibility of diapirism of ultramafic-rich mélanges if the densities, viscosities, thicknesses of the mélange and the subduction timescales are well constrained for each subduction zone.

4.4. Slab tear and partial melting of ultramafic-rich mélanges

The wet solidus of serpentine-rich mélanges (~1050–1100 °C) from deep fore-arc to sub-arc depths is higher than the hottest slab-top geotherm (Fig. 5), implying that they would rarely melt in cold to hot subduction zones but would dehydrate to form olivine-pyroxenites with minor mica and amphiboles (±garnet ±oxides). Similarly, chlorite-rich mélanges would rarely melt in cold to intermediate subduction zones (except in hotter slab geotherms), contributing to aqueous fluids into the mantle wedge.

A potential geodynamic scenario that could add substantial heat to the ultramafic-rich mélanges is the interaction with the hotter asthenosphere through slab tears, which are well documented through geophysical observations in convergent plate boundaries such as the Marianas (e.g., Miller et al., 2006), Kamchatka (e.g., Levin et al., 2002), Cocos (e.g., Castellanos et al., 2018), Nazca (e.g., Rodríguez et al., 2024) and the Central Apennine (Rosenbaum et al., 2008). They generally involve the rollback of parts of the slab followed by the segmentation of the subduction zone through slab tearing, creating 'windows' where the upwelling hot asthenosphere intrudes (e.g., toroidal flow) and interacts with the mélange channel (Fig. 6a). Another geodynamic scenario is the ascent of mélange diapirs into the hotter mantle (Fig. 6b). However, serpentine-rich mélange diapirs are unlikely to occur since they densify at temperatures as low as ~700 °C (Fig. 3) and would require exceptional conditions, as discussed in Section 4.3. In addition, melting of serpentine-rich mélanges would produce iron-rich basaltic magmas (~47–53 wt.% SiO_2, ~11–17 wt.% FeO) that are significantly enriched in MgO (11–21 wt.%) and depleted in alkalis (~0.5–3 wt.%), CaO (~0.8–5 wt.%), TiO_2 (~0.1–0.5 wt.%) and relatively low in Al_2O_3 (10–18 wt.%) compared to global basaltic arc magmas that show high alkalis (~1–4.5 wt.%), CaO (~7.5–15 wt.%), TiO_2 (~0.5–2 wt.%), Al_2O_3 (~12–22 wt.%) but lower in MgO (~2–18 wt.%) (Fig. 7). Also, the K_2O/H_2O ratios of serpentine-rich mélange partial melts from this study (~0.01–0.04) are far from those of arc basalts (0.05–0.4) (Hermann and Spandler, 2008). Thus, formation of basaltic arc magmas from serpentine-rich mélange sources requires the interaction of these primary magmas with sources rich in alkalis, CaO, and TiO_2, Al_2O_3 such as carbonaceous materials (Ducea et al., 2022), the oceanic crust (Rapp and Watson, 1995), or a more enriched peridotitic mantle (Grove and Till, 2019). On the other hand, low-density chlorite-rich mélanges may favor diapirism (Lakey and Hermann, 2022; Codillo et al., 2023), and from a major element perspective, the magmas produced from chlorite-rich mélange melting may resemble alkaline and calc-alkaline arc magmas, except for the higher alkali and lower FeO contents than global arc magmas (Figure S10).

4.5. Implications for chemical geodynamics

The dehydration or melting of ultramafic-rich mélanges (serpentine or chlorite-rich) would affect the budget of fluid-mobile elements (i.e. LILE), Large Ion Lithophile Elements (LILEs), volatiles, and fluid-immobile elements (i.e. High Field Strength Elements, HFSE) in the mantle wedge. In this section, we assess whether the contribution of ultramafic-rich mélanges to arc magmatism sources may produce the

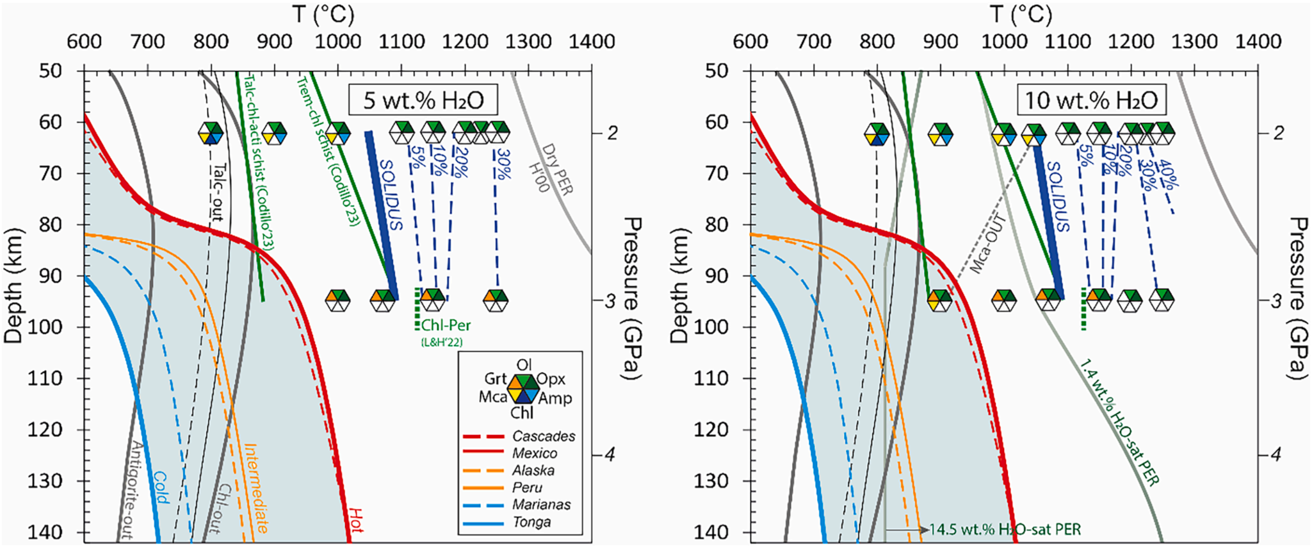

Fig. 5. Phase equilibria of serpentine-rich matrices in *P-T* space at 5 and 10 wt.% bulk H_2O. The inferred *T*-solidus of serpentine-rich matrices from forearc to subarc depths (~65–95 km) is located between 1050 and 1100 °C and is represented by a thick blue solid line. The navy-blue dashed lines indicate the melt fraction (*F%*) inferred by mass balance calculations. The solidus for chlorite-rich mélanges from Codillo et al. (2023) and Lakey and Hermann (2022) are represented with green solid lines and green dashed-line, respectively. The solidus for dry (Hirschmann, 2000), water-saturated peridotite at 1.4 wt.% H_2O (Green et al., 2014), and water-saturated peridotite at 14.5 wt.% H_2O (Till *et al.*, 2012) are shown for reference. The stability curves of the antigorite (Ulmer and Trommsdorff, 1995) and chlorite (Lakey and Hermann, 2022) are also shown. The dashed black line and the solid black line indicate the talc stability from Pawley and Wood (1995) and Bose and Ganguly (1995), respectively. The blue arrows indicate the release of aqueous fluids. The slab geotherms are retrieved from Syracuse et al. (2010). Mineral abbreviations are: Ol, olivine; Opx, orthopyroxene; Grt, garnet; Mca, mica; Amp, amphibole; Chl, chlorite.

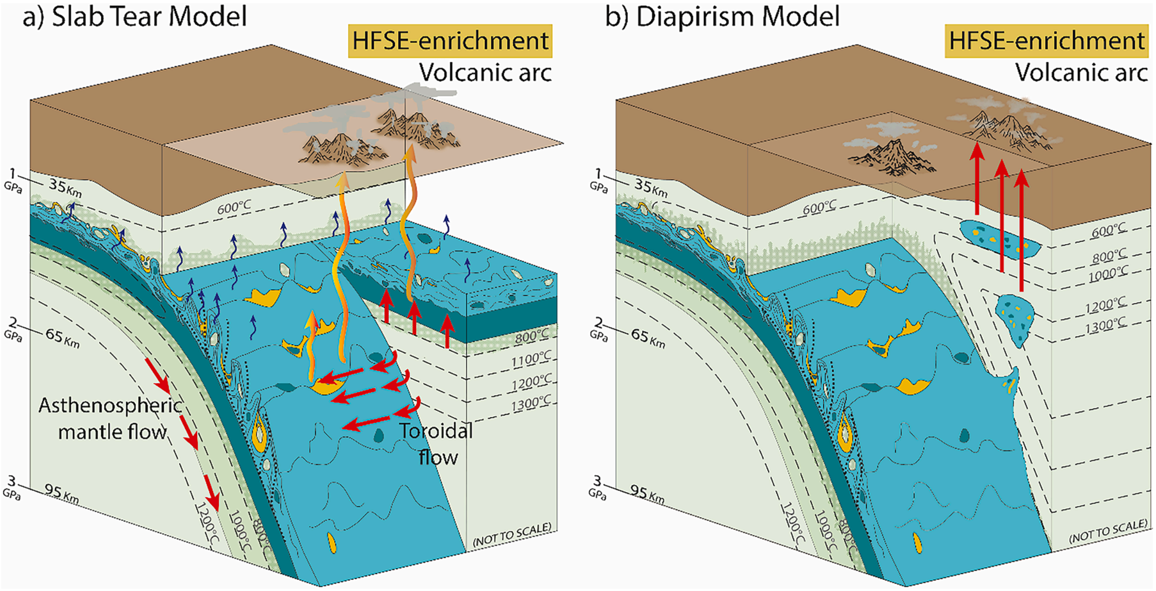

Fig. 6. Two potential geodynamic scenarios of mass transfer (e.g., HFSE) from ultramafic-rich mélanges to arc sources: (a) Toroidal flow of the hot asthenosphere (red arrows) through a slab tear; (b) ascent of mélange diapirs into the hotter mantle wedge. In both scenarios, the melting of Ti-rich and HFSE-bearing phases (e.g., rutile, spinel, oxides) that transfer HFSE-rich signatures to arc sources is implied, which would not produce the HFSE-depletion observed in arc lavas worldwide (compared to MORB).

ubiquitous high LILE/HFSE signatures observed in arc magmas globally.

Low density serpentine-rich mélanges may sustain a positive buoyancy until the breakdown of antigorite at ~80 km depth for hot-intermediate subduction zones and at ~110 km for cold subduction zones (Fig. 5) as long as the mélange does not thermally equilibrate at $T \geq 800$ °C (Fig. 3), resulting in 'failed diapirs' or 'detached stalled diapirs' (Fig. 8). The dehydration and densification process is also relevant for most chlorite-rich mélange channels. Chlorite breakdown at >80 km for hot-intermediate subduction zones and >140 km for cold subduction zones (Fig. 5) suggests that chlorite-rich mélanges can sustain their buoyancy at greater depths if they meet the criteria discussed in Section 4.3 and do not reach thermal equilibration at $T \geq 1000$ °C (Fig. 5). The thermal structure of the subduction zone also may impact how the mélange diapir travels into the mantle wedge. In cold subduction zones, the slab-top isotherms are more closely spaced than in hot subduction zones (Fig. 8a and b). Serpentine- and chlorite-rich mélanges lose their buoyancy at ≥800 °C and >1000 °C respectively, hence, the rising diapirs would have an even shorter journey before they stall and are

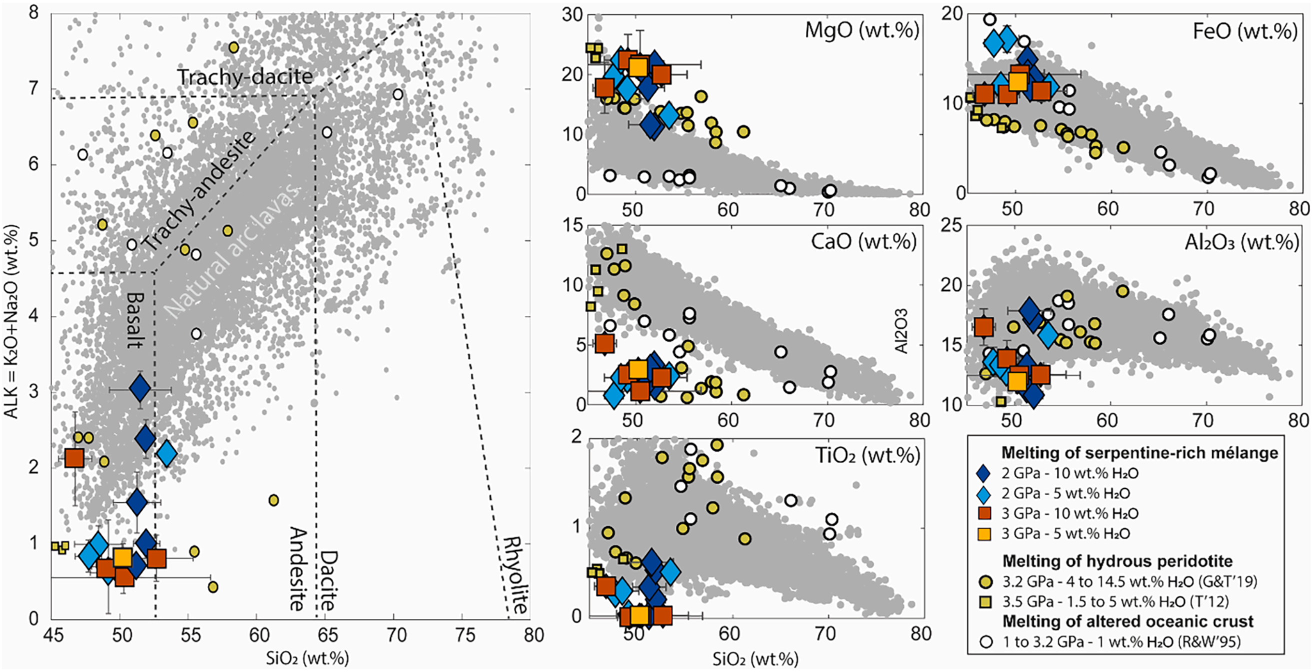

Fig. 7. Element oxides vs. SiO_2 of serpentinite-rich mélange partial melts relative to global natural arc lavas (arc data from Straub, 2017; and GeoROC Database). The compositions are volatile-free. The error bars are smaller than the symbol sizes for specific data points.

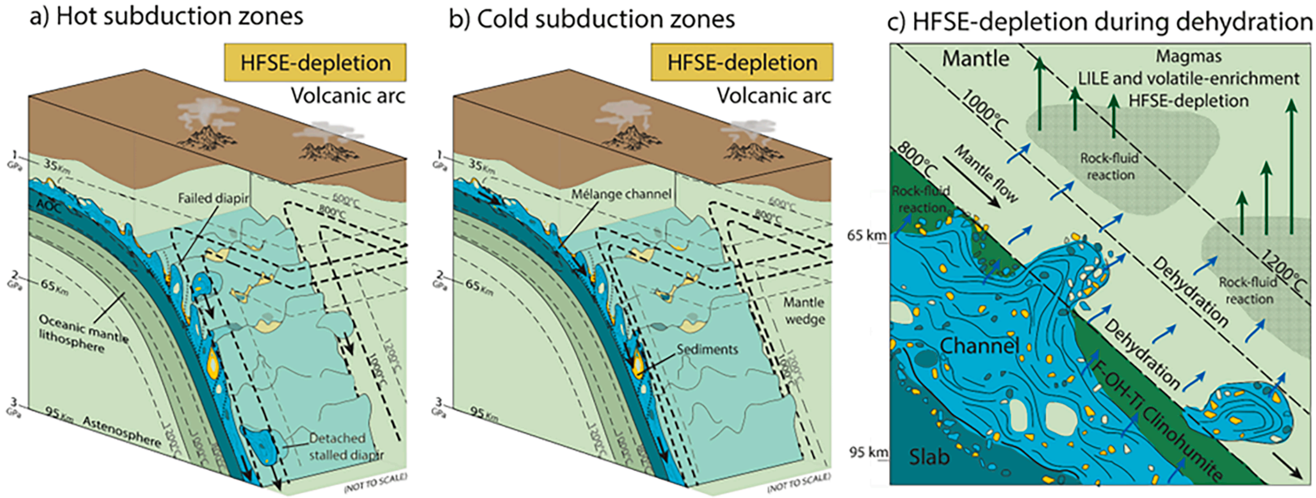

Fig. 8. Representation of the potential fate of ultramafic-rich mélanges in (a) hot and (b) cold subduction zones (Not to scale). In hot subduction zones (a), the buoyancy of serpentine- and chlorite-rich matrices are limited to temperatures <800 °C and <1000 °C, respectively, as they can form failed diapirs (still attached to the channel) or detached stalled diapirs. In cold subduction zones (b), the mantle isotherms are closer to the slab-top, and any diapir would stall even earlier. Dehydration of ultramafic-rich mélanges releases LILES and volatiles through aqueous fluids (blue arrows) as they are dragged beyond sub-arc depths by the ambient flow (black arrows), although cold channels can carry more LILES, volatiles, and HFSE more effectively beyond subarc depth. (c) Schematic cartoon (not to scale) of the fluids derived from the ultramafic-mélanges interacting with the overlying mantle (rock-fluid reaction) and forming a reacted layer of F-OH-Ti clinohumite that acts as a sink of HFSE (Garrido et al., 2005). The aqueous fluids released from this layer would interact with overlying peridotite rocks and further enhance HFSE depletion. Consequently, the HFSE depletion (or high LILE/HFSE ratio) signature is transferred to arc magma sources located in hotter domains in the mantle wedge (>1000 °C).

dragged by the ambient flow into the deep mantle carrying larger fractions of LILE, HFSE and volatiles (e.g., N, H, O) compared to hotter slabs (Fig. 8). As the temperature increases, the dehydration of serpentine-rich mélange channels forms a residual olivine-pyroxenite that contains minor amphibole, mica, and Fe-Al-Ti-oxides. To assess the effect of dehydration on LILE and HFSE fractionation, we modeled the LILE/HFSE ratio in the aqueous fluid using the mineral phase proportions (wt.%) from this study and mineral-fluid partition coefficients from the literature (Figure S11; *Table S14*). We find that at 2 GPa and up to 1000 °C, the solid mineral residue (K/Nb=2462; Rb/Nb=10) has a similar LILE/HFSE ratio as the mélange (K/Nb=2624; Rb/Nb=10) due to the presence of amphibole, mica and the oxides that hold back a large fraction of LILEs and HFSEs. The residual oxide minerals have a very strong preference for HFSE resulting in aqueous fluids enriched in LILE relative to HFSE (K/Nb=19,289; Rb/Nb=51). Some fraction of volatiles can still be carried by micas and amphiboles at $T \leq 1050$ °C (Ulmer and Trommsdorff, 1995) and by nominally anhydrous minerals into the deep mantle (Kovács et al., 2012). At 3 GPa, residual amphibole and mica are not present at 1000 °C thereby enhancing the LILE/HFSE ratio in the released aqueous fluid (K/Nb=44,134; Rb/Nb=172). Similarly, chlorite-rich mélanges contain accessory minerals that have a strong preference for HFSE (titanite, rutile, ilmenite, zircon) and would release aqueous fluids into the mantle with high LILE/HFSE ratios. Nonetheless, the presence of fluorine enhances the solubility of HFSE in aqueous fluids (Keppler, 1996). Such fluid-mantle interaction may favor the precipitation of Fe-Ti-oxides and F-OH-Ti-clinohumite intergrowths that act as HFSE sinks, depleting the aqueous fluids of HFSE without changing the LILE content (Garrido et al., 2005; López Sánchez-Vizcaíno et al., 2005; and references therein; Fig. 8c). Therefore, fractionation of LILE from HFSE can occur at or near the slab channel during dehydration processes. Partial melting of arc sources due to the flux of high LILE/HFSE bearing aqueous fluids can produce the high LILE/HFSE ratios ubiquitously observed in arc magmas worldwide.

If the timescale of diapir ascent is faster than the timescale of thermal diffusion and mineralogical equilibration, the core of the diapir can still be positively buoyant and make its way from the slab-top through the hotter mantle wedge. To assess the effect of partial melting on HFSE fractionation, we performed batch melting modeling using the phase proportions (wt.%) from this experimental study and mineral-melt partition coefficient from the literature (Supplementary Information S6; Table S15). Our results show that as long as there are no residual oxides/rutile at ≥1100 °C, the resultant melts preserve the same trace element signature (Rb/Nb=10; Nb/Ta=13) as the pre-molten mélange (Rb/Nb=10; Nb/Ta=13) at both 2 and 3 GPa. Overall, if the ultramafic-rich mélange had an initial high LILE/HFSE ratio (e.g., serpentinites from Syros) or lower LILE/HFSE ratio (e.g., chlorite-rich mélange from Cerro del Almirez), the resultant partial melts would mirror that signature (Figure S12). The infiltration of those partial melts through the overriding hotter mantle wedge would result in the formation of orthopyroxenites (Rebaza et al., 2023) without forming any Fe-Ti-oxides (Mallik et al., 2016). Thus, it is likely that the LILE/HFSE ratio signature in the percolating melt remains unaffected during reactive transport through the hotter mantle wedge.

Slab tears and interaction with hotter asthenosphere can partially melt ultramafic-rich mélanges. If the asthenosphere is OIB-like and likely HFSE enriched, such interactions may lead to the gain of HFSEs in the mélange partial melts thus lowering the LILE/HFSE ratios in the resultant melt (Liu *et al.*, 2024). For interactions with asthenosphere that has undergone prior episodes of melt extraction and are not HFSE enriched, the mélange partial melts would reflect high LILE/HFSE ratio. Interaction of a dehydrated mélange (low LILE/HFSE ratios) with a hotter asthenosphere would result in low LILE/HFSE ratios in the partial melts. Only if the mélange is not yet dehydrated, the interaction with the asthenosphere will result in high LILE/HFSE ratios in the resultant melt. Overall, partial melting of ultramafic-rich mélanges due to diapiric rise to the sub-arc mantle or due to interaction with the hotter asthenosphere through slab tears has been attributed to HFSE enrichment signatures (Liu et al., 2024; Rosenbaum et al., 2008) but not the near ubiquitous high LILE/HFSE ratios. Assuming that ultramafic-rich mélanges contribute to the source of primary arc basalts, the characteristic high LILE/HFSE ratios compared to that of MORBs may be best explained by the following: (a) Dehydration of ultramafic-rich mélanges along the slab or in a failed or stalled diapir close to the slab-mantle boundary, and the formation of Fe-Ti-oxides and F-OH-Ti-clinohumite in the wedge chlorite-harzburgite that scavenges the HFSE from the aqueous fluids; (b) partial melting of ultramafic-rich mélanges with pre-existing high LILE/HFSE ratios due to diapiric ascent to the hotter mantle wedge or due to slab tear (but with limited HFSE gain from the influx of asthenosphere through the tear). Given high LILE/HFSE ratio is a ubiquitous arc magma signature, but slab tears are not, and diapirism in ultramafic-rich mélanges is highly conditional, our study indicates that aqueous fluids are the dominant metasomatic agent that transfer ultramafic-rich slab components into mantle sources (e.g., LILEs, volatiles) rather than diapirs.

5. Conclusions

This study provides the mineral assemblage and the associated density transformation of hydrous serpentine-rich mélange matrix and compares it with chlorite-rich matrices from the literature to assess the buoyancy of ultramafic-rich mélanges from fore-arc to sub-arc depths. The solidus temperature of serpentine-rich mélanges under fore-arc to sub-arc conditions is higher than all slab-top geotherms. This implies that the matrices would partially melt only under specific geodynamic conditions such as slab tear or diapiric ascent into the hotter mantle wedge, although the partial melts do not resemble the compositions of arc lavas. We show that serpentine- and chlorite-rich mélanges dehydrate as they subduct and lose their buoyancy at ≥ 800 °C and > 1000 °C, respectively. This implies that even if a diapir initiates it would continue its ascent into the hotter mantle wedge only if the ascent timescales are faster than the timescales of thermal diffusion and mineralogical equilibration, such that at least the core of the diapir may still retain its positive buoyancy. Furthermore, diapir initiation in cold subduction channels require thicker mélanges compared to their hotter counterparts, for a given density contrast (with the surrounding mantle) and viscosity. At higher viscosities, the required channel thicknesses in cold slabs may exceed the observed thickness for subduction channels implying that diapirism would not commonly occur. Overall, our assessment concludes that diapirism in ultramafic-rich mélanges is feasible only when a specific set of conditions are met and may not be common. Dehydration of ultramafic-rich mélanges and release of aqueous fluids to arc sources would fractionate LILEs from HFSEs by fluid-rock reaction and precipitation of minerals such as F-OH-Ti-clinohumite that sequester HFSEs, therefore imparting the high LILE/HFSE ratios ubiquitously observed in arc magmas. On the other hand, partial melting of ultramafic-rich mélange due to slab tear or diapirism would not fractionate HFSEs from LILEs and impart the LILE/HFSE signature of the subducted ultramafic-rich mélange. Therefore, the partial melts would produce high LILE/HFSE ratios in resultant arc magmas only if the ultramafic-rich mélange had a high LILE/HFSE ratio before the onset of melting. As the majority of arc magmas show a distinct HFSE depletion (relative to MORB), and slab tears are not common place, and diapirism in ultramafic-rich mélanges is only feasible when a specific set of conditions are met, our study corroborates that aqueous fluids released from ultramafic-rich mélanges are the predominant metasomatic agent that transfer slab components into arc sources rather than diapirs.

Funding

AMR acknowledges the David J. Lowell Scholarship and GPSC Research and Project Grant. AM acknowledges the National Science Foundation grant EAR 2138410. BIH acknowledges the M. Lee Allison Scholarship by the Arizona Geological Society. We acknowledge NASA grants #80NSSC23K0327, #NNX12AL47G, #NNX15AJ22G and #NNX07AI520, and NSF grants #1531243 and #EAR-0841669 for funding of the instrumentation in the Kuiper-Arizona Laboratory for Astromaterials Analysis at the University of Arizona.

CRediT authorship contribution statement

Anna M. Rebaza: Writing – original draft, Visualization, Methodology, Investigation, Formal analysis, Data curation, Conceptualization. **Ananya Mallik:** Writing – review & editing, Supervision, Methodology, Funding acquisition, Conceptualization. **Emily H.G. Cooperdock:** Writing – review & editing, Supervision. **Bridgett I. Holman:** Investigation.

Declaration of competing interest

All co-authors, after a thorough review, have unanimously agreed on the re-submission of the manuscript to the journal. We confirm that this work has not been published, submitted, or under consideration for publication elsewhere. We have no conflicts of interest to disclose.

Data availability

The data is uploaded as attached file.

Acknowledgments

We are grateful for the insightful comments from Dr. Jörg Hermann and an anonymous reviewer that strengthened and enriched this work, and Dr. Rosemary Hickey-Vargas for handling the manuscript. We thank Zachary Michels and Tristan Nolan for their assistance with the SEM and Ken Domanik for his assistance with the EMPA. We thank Arkadeep Roy, Emilie Bowman, Isaiah Spring, Justine Grabiec, and Ailani Bonilla for the helpful discussions. We also want to thank Paul Asimow and Paula Antoshechkina for offering a workshop on alphaMELTS at the University of Arizona and for the discussions during the workshop. Lastly, we want to thank the team of undergraduate researchers from the Mallik Petrology Group for preparing essential assembly materials for the experiments.

Supplementary materials

Supplementary material associated with this article can be found, in the online version, at doi:10.1016/j.epsl.2024.119020.

References

Abers, G.A., van Keken, P.E., Wilson, C.R., 2020. Deep decoupling in subduction zones: observations and temperature limits. Geosphere 16, 1408–1424. https://doi.org/10.1130/GES02278.1.

Abers, G.A., 2005. Seismic low-velocity layer at the top of subducting slabs: observations, predictions, and systematics. Phys. Earth Planet. Inter. 149, 7–29.

Behn, M.D., Kelemen, P.B., Hirth, G., Hacker, B.R., Massonne, H.J., 2011. Diapirs as the source of the sediment signature in arc lavas. Nat. Geosci. 4, 641–646. https://doi.org/10.1038/ngeo1214.

Blanco-Quintero, I.F., Proenza, J.A., García-Casco, A., Tauler, E., Galí, S., 2011. Serpentinites and serpentinites within a fossil subduction channel: la Corea mélange, eastern Cuba. Geol. Acta 9, 389–405. https://doi.org/10.1344/105.00000166.

Bose, K., Ganguly, J., 1995. Experimental and theoretical studies of the stabilities of talc, antigorite and phase A at high pressures with applications to subduction processes. Earth Planet. Sci. Lett. 136, 109–121.

Breeding, C.M., Ague, J.J., Bröcker, M., 2004. Fluid-metasedimentary rock interactions in subduction-zone mé lange: implications for the chemical composition of arc magmas. Geology 32, 1041–1044. https://doi.org/10.1130/G20877.1.

Butjosa, L., Cambeses, A., Proenza, J.A., Agostini, S., Iturralde-Vinent, M., Bernal-Rodríguez, L., Garcia-Casco, A., 2023. Relict abyssal mantle in a Caribbean forearc ophiolite (Villa Clara, central Cuba): petrogenetic and geodynamic implications. Int. Geol. Rev. https://doi.org/10.1080/00206814.2023.2179229.

Castellanos, J.C., Clayton, R.W., Pérez-Campos, X., 2018. Imaging the Eastern Trans-Mexican volcanic belt with ambient seismic noise: evidence for a slab tear. J. Geophys. Res. Solid Earth 123, 7741–7759. https://doi.org/10.1029/2018JB015783.

Castro, A., Gerya, T., García-Casco, A., Fernández, C., Díaz-Alvarado, J., Moreno-Ventas, I., Löw, I., 2010. Melting relations of MORB-sediment mélanges in underplated mantle wedge plumes; Implications for the origin of Cordilleran-type batholiths. J. Petrol. 51, 1267–1295. https://doi.org/10.1093/petrology/egq019.

Cloos, M., Shreve, R.L., 1988. Subduction-channel model of prism accretion, melange formation, sediment subduction, and subduction erosion at convergent plate margins: 1. Background and description. pure Appl. Geophys. 128, 455–500. https://doi.org/10.1007/BF00874548.

Codillo, E.A., Le Roux, V., Marschall, H.R., 2018. Arc-like magmas generated by mélange-peridotite interaction in the mantle wedge. Nat. Commun. 9, 1–11. https://doi.org/10.1038/s41467-018-05313-2.

Codillo, E.A., Le Roux, V., Klein, B., Behn, M.D., Marschall, H.R., Bebout, G.E., 2023. The ascent of subduction zone mélanges: experimental constraints on mélange rock densities and solidus temperatures. Earth Planet. Sci. Lett. 621. https://doi.org/10.1016/j.epsl.2023.118398.

Coleman, R.G., 1971. Petrologic and geophysical nature of serpentinites. Geol. Soc. Am. Bull. 82, 897–918. https://doi.org/10.1130/0016-7606(1971)82[897:PAGNOS]2.0.CO;2.

Cooperdock, E.H.G., Raia, N.H., Barnes, J.D., Stockli, D.F., Schwarzenbach, E.M., 2018. Tectonic origin of serpentinites on Syros, Greece: geochemical signatures of abyssal origin preserved in a HP/LT subduction complex. Lithos 296–299, 352–364. https://doi.org/10.1016/j.lithos.2017.10.020.

Cruz-Uribe, A.M., Marschall, H.R., Gaetani, G.A., Le Roux, V., 2018. Generation of alkaline magmas in subduction zones by partial melting of mélange diapirs-An experimental study. Geology 46, 343–346. https://doi.org/10.1130/G39956.1.

Davis, F.A., Hirschmann, M.M., Humayun, M., 2011. The composition of the incipient partial melt of garnet peridotite at 3GPa and the origin of OIB. Earth Planet. Sci. Lett. 308, 380–390. https://doi.org/10.1016/j.epsl.2011.06.008.

Ducea, M.N., Currie, C.A., Balica, C., Lazar, I., Mallik, A., Petrescu, L., Vlasceanu, M., 2022. Diapirism of carbonate platforms subducted into the upper mantle. Geology 50, 929–933. https://doi.org/10.1130/G50000.1.

Elliott, T., Plank, T., Zindler, A., White, W., Bourdon, B., 1997. Element transport from slab to volcanic front at the Mariana arc. J. geophy 102, 14,991-15,018.

Garrido, C.J., López Sánchez-Vizcaíno, V., Gómez-Pugnaire, M.T., Trommsdorff, V., Alard, O., Bodinier, J.L., Godard, M., 2005. Enrichment of HFSE in chlorite-harzburgite produced by high-pressure dehydration of antigorite-serpentinite: Implications for subduction magmatism. Geochem. Geophys. Geosyst. 6, 1–15. https://doi.org/10.1029/2004GC000791.

Geersen, J., 2019. Sediment-starved trenches and rough subducting plates are conducive to tsunami earthquakes. Tectonophysics 762, 28–44. https://doi.org/10.1016/j.tecto.2019.04.024.

Gerya, T.V., Yuen, D.A., 2003. Rayleigh - Taylor instabilities from hydration and melting propel "cold plumes" at subduction zones. Earth Planet. Sci. Lett. 212, 47–62. https://doi.org/10.1016/S0012-821X(03)00265-6.

Ghiorso, M.S., Hirschmann, M.M., Reiners, P.W., Kress, V.C., 2002. The pMELTS: a revision of MELTS for improved calculation of phase relations and major element partitioning related to partial melting of the mantle to 3 GPa. Geochem., Geophys. Geosyst. 3, 1–35. https://doi.org/10.1029/2001 gc000217.

Green, D.H., Hibberson, W.O., Rosenthal, A., Kovács, I., Yaxley, G.M., Falloon, T., Brink, F., 2014. Experimental study of the influence of water on melting and phase assemblages in the upper mantle. J. Petrol. 55, 2067–2096. https://doi.org/10.1093/petrology/egu050.

Grigull, S., Krohe, A., Moos, C., Wassmann, S., Stöckhert, B., 2012. Order from chaos": a field-based estimate on bulk rheology of tectonic mélanges formed in subduction zones. Tectonophysics 568–569, 86–101. https://doi.org/10.1016/j.tecto.2011.11.004.

Grove, T.L., Till, C.B., 2019. H2O-rich mantle melting near the slab–wedge interface. Contrib. Mineral. Petrol. 174, 1–22. https://doi.org/10.1007/s00410-019-1615-1.

Hawkesworth, C.J., Turner, S.P., McDermott, F., Peate, D.W., Van Calsteren, P., 1997. U-Th isotopes in arc magmas: implications for element transfer from the subducted crust. Science (80-.) 276, 551–555. https://doi.org/10.1126/science.276.5312.551.

Hermann, J., Spandler, C.J., 2008. Sediment melts at sub-arc depths: an experimental study. J. Petrol. 49, 717–740. https://doi.org/10.1093/petrology/egm073.

Hermann, J., Müntener, O., Scambelluri, M., 2000. The importance of serpentinite mylonites for subduction and exhumation of oceanic crust. Tectonophysics 327, 225–238. https://doi.org/10.1016/S0040-1951(00)00171-2.

Hirschmann, M.M., 2000. Mantle solidus: experimental constraints and the effects of peridotite composition. Geochem., Geophys. Geosyst. 1. https://doi.org/10.1029/2000GC000070.

Hirth, G., Kohlstedt, D.L., 2003. Rheology of the upper mantle and the mantle wedge: a view from the experimentalists BT. Geophys. Monogr. Ser. 138, 83–106.

Ho, C.Q., 2019. Conditions of Mélange Diapir Formation. University of Maryland.

Horleston, A.C., Helffrich, G.R., 2012. Constraining sediment subduction: a converted phase study of the Aleutians and Marianas. Earth Planet. Sci. Lett. 359–360, 141–151. https://doi.org/10.1016/j.epsl.2012.10.019.

Kelemen, P.B., Johnson, K.T.., Kinzler, R.J., Irving, A.J., 1990. High-field-strength element depletions in arc basalts due to mantle-magma interaction 345, 521–524.

Keppler, H., 1996. Constraints from partitioning experiments on the composition of subduction-zone fluids. Nature 380, 237–240. https://doi.org/10.1038/380237a0.

Kessel, R., Schmidt, M.W., Ulmer, P., Pettke, T., 2005. Trace element signature of subduction-zone fluids, melts and supercritical liquids at 120-180 km depth. Nature 437, 724–727. https://doi.org/10.1038/nature03971.

Kovács, I., Green, D.H., Rosenthal, A., Hermann, J., O'neill, H.S.C., Hibberson, W.O., Udvardi, B., 2012. An experimental study of water in nominally anhydrous minerals in the upper mantle near the water-saturated solidus. J. Petrol. 53, 2067–2093. https://doi.org/10.1093/petrology/egs044.

Lázaro, C., García-Casco, A., 2008. Geochemical and Sr-Nd isotope signatures of pristine slab melts and their residues (Sierra del Convento mélange, eastern Cuba). Chem. Geol. 255, 120–133. https://doi.org/10.1016/j.chemgeo.2008.06.017.

López Sánchez-Vizcaíno, V., Trommsdorff, V., Gómez-Pugnaire, M.T., Garrido, C.J., Müntener, O., Connolly, J.A.D., 2005. Petrology of titanian clinohumite and olivine at the high-pressure breakdown of antigorite serpentinite to chlorite harzburgite (Almirez Massif, S. Spain). Contrib. to Mineral. Petrol. 149, 627–646. https://doi.org/10.1007/s00410-005-0678-3.

Lakey, S., Hermann, J., 2022. An experimental study of chlorite stability in varied subduction zone lithologies with implications for fluid production, melting, and diapirism in chlorite-rich melange rocks. J. Petrol. 63, 1–29. https://doi.org/10.1093/petrology/egac029.

Levin, V., Shapiro, N., Park, J., Ritzwoller, M., 2002. Seismic evidence for catastrophic slab loss beneath Kamchatka. Nature 418, 763–767. https://doi.org/10.1038/nature00973.

Lin, C.H., Shih, M.H., Lai, Y.C., 2021. Mantle wedge diapirs detected by a dense seismic array in Northern Taiwan. Sci. Rep. 11, 1–12. https://doi.org/10.1038/s41598-021-81357-7.

Liu, H., Hastie, A.R., Petrone, C.M., 2024. High-field-strength-element enriched arc rocks witness subducted mélange recycling in upwelling asthenosphere. Lithos 464–465. https://doi.org/10.1016/j.lithos.2023.107411.

Mallik, A., Nelson, J., Dasgupta, R., 2015. Partial melting of fertile peridotite fluxed by hydrous rhyolitic melt at 2–3 GPa: implications for mantle wedge hybridization by sediment melt and generation of ultrapotassic magmas in convergent margins. Contrib. Mineral. Petrol. 169. https://doi.org/10.1007/s00410-015-1139-2.

Mallik, A., Dasgupta, R., Tsuno, K., Nelson, J., 2016. Effects of water, depth and temperature on partial melting of mantle-wedge fluxed by hydrous sediment-melt in subduction zones. Geochim. Cosmochim. Acta 195, 226–243. https://doi.org/10.1016/j.gca.2016.08.018.

Marschall, H.R., Schumacher, J.C., 2012. Arc magmas sourced from mélange diapirs in subduction zones. Nat. Geosci. 5, 862–867. https://doi.org/10.1038/ngeo1634.

Miller, D.M., Goldstein, S.L., Langmuir, C.H., 1994. Cerium/lead and lead isotope ratios in arc magmas and the enrichment of lead in the continents. Nature 368, 514–520.

Miller, M.S., Gorbatov, A., Kennett, B.L.N., 2006. Three-dimensional visualization of a near-vertical slab tear beneath the southern Mariana arc. Geochem., Geophys. Geosyst. 7, 1–8. https://doi.org/10.1029/2005GC001110.

Nielsen, S.G., Marschall, H.R., 2017. Geochemical evidence for mélange melting in global arcs. Sci. Adv. 3, 1–7. https://doi.org/10.1126/sciadv.1602402.

Pawley, A.R., Wood, B.J., 1995. The high-pressure stability of talc and 10 Å phase: potential storage sites for H2O in subduction zones. Am. Mineral. 80, 998–1003. https://doi.org/10.2138/am-1995-9-1015.

Penniston-Dorland, S.C., Harvey, K.M., 2023. Geosystems and geoenvironment Constraints on tectonic processes in subduction mélange : a review of insights from the Catalina Schist (CA, USA). Geosyst. Geoenviron. 2. https://doi.org/10.1016/j.geogeo.2023.100190.

Platt, J.P., 2015. Origin of Franciscan blueschist-bearing melange at San Simeon, central California coast. Int. Geol. Rev. 57, 843–853. https://doi.org/10.1080/00206814.2014.902756.

Raia, N.H., Whitney, D.L., Teyssier, C., Lesimple, S., 2022. Serpentinites of different tectonic origin in an exhumed subduction complex (New Caledonia, SW Pacific). Geochem., Geophys. Geosyst. 23, 1–31. https://doi.org/10.1029/2022GC010395.

Rapp, P., Watson, B., 1995. Dehydration melting of metabasalt at 8-32 kbar: implications for continental growth and crust - mantle recycling. J. Petrol. 36, 891–931.

Rebaza, A.M., Mallik, A., Straub, S.M., 2023. Multiple episodes of rock-melt reaction at the slab-mantle interface: formation of high silica primary magmas in intermediate to hot subduction zones. J. Petrol. 1–20. https://doi.org/10.1093/petrology/egad011.

Rodríguez, E.E., Beck, S.L., Ruiz, M., Meltzer, A., Portner, D.E., Hernández, S., Segovia, M., Agurto-Detzel, H., Charvis, P., 2024. Seismic imaging of the northern andean subduction zone from teleseismic tomography: a torn and fragmented nazca slab. Geophys. J. Int. 236, 593–606. https://doi.org/10.1093/gji/ggad421.

Rosenbaum, G., Gasparon, M., Lucente, F.P., Peccerillo, A., Miller, M.S., 2008. Kinematics of slab tear faults during subduction segmentation and implications for Italian magmatism. Tectonics 27, 1–16. https://doi.org/10.1029/2007TC002143.

Sadofsky, S.J., Bebout, G.E., 2003. Record of forearc devolatilization in low-T, high-P/T metasedimentary suites: significance for models of convergent margin chemical cycling. Geochem., Geophys. Geosyst. 4, 1–29. https://doi.org/10.1029/2002GC000412.

Shreve, R.L., Cloos, M., 1986. Dynamics of sediment subduction, melange formation, and prism accretion. J. Geophys. Res. 91, 10229–10245. https://doi.org/10.1029/jb091ib10p10229.

Sorensen, S.S., Grossman, J.N., 1993. Accessory minerals and subduction zone metasomatism : a geochemical comparison of two melanges (Washington and California, U.S.A). Chem. Geol. 110, 269–297.

Spandler, C., Hermann, J., Faure, K., Mavrogenes, J.A., Arculus, R.J., 2008. The importance of talc and chlorite “hybrid” rocks for volatile recycling through subduction zones; evidence from the high-pressure subduction mélange of New Caledonia. Contrib. Mineral. Petrol. 155, 181–198. https://doi.org/10.1007/s00410-007-0236-2.

Straub, S.M., Gómez-Tuena, A., Bindeman, I.N., Bolge, L.L., Brandl, P.A., Espinasa-Perena, R., Solari, L., Stuart, F.M., Vannucchi, P., Zellmer, G.F., 2015. Crustal recycling by subduction erosion in the central Mexican Volcanic Belt. Geochim. Cosmochim. Acta 166, 29–52. https://doi.org/10.1016/j.gca.2015.06.001.

Straub, S.M., (2017). Compilation of published major and trace elements and Sr-Nd-Pb-Hf isotope ratios of Quaternary-age arc volcanic rocks from 9 arc settings, Version 1.0. Interdiscip. Earth Data Alliance (IEDA). https://doi.org/10.1594/IEDA/100664.

Syracuse, E.M., van Keken, P.E., Abers, G.A., Suetsugu, D., Bina, C., Inoue, T., Wiens, D., Jellinek, M., 2010. The global range of subduction zone thermal models. Phys. Earth Planet. Inter. 183, 73–90. https://doi.org/10.1016/j.pepi.2010.02.004.

Till, C.B., Grove, T.L., Withers, A.C., 2012. The beginnings of hydrous mantle wedge melting. Contrib. Mineral. Petrol. 163, 669–688. https://doi.org/10.1007/s00410-011-0692-6.

Trotet, F., Vidal, O., Jolivet, L., 2001. Exhumation of Syros and Sifnos metamorphic rocks (Cyclades, Greece). New constraints on the P-T paths. Eur. J. Mineral. 13, 901–920. https://doi.org/10.1127/0935-1221/2001/0013/0901.

Turcotte, DL, Schubert, G, 2014. Geodynamics, 3rd edn. Cambridge University Press, Cambridge, UK, p. 623.

Ukar, E., Cloos, M., 2019. Cataclastic deformation and metasomatism in the subduction zone of mafic blocks-in-mélange, San Simeon, California. Lithos 346–347. https://doi.org/10.1016/j.lithos.2019.06.018.

Ulmer, P., Trommsdorff, V., 1995. Serpentine stability to mantle depths and subduction-related magmatism. Science (80-.) 268, 858–861. https://doi.org/10.1126/science.268.5212.858.

Walowski, K.J., Wallace, P.J., Hauri, E.H., Wada, I., Clynne, M.A., 2015. Slab melting beneath the Cascade Arc driven by dehydration of altered oceanic peridotite. Nat. Geosci. 8, 404–408. https://doi.org/10.1038/ngeo2417.

Xu, Y., 2000. Distribution of trace elements in spinel and garnet peridotites. Sci. China, Ser. D Earth Sci. 43, 166–175. https://doi.org/10.1007/BF02878146.

Zhang, J., 2020. The study of subduction channels: progress, controversies, and challenges. Sci. China Earth Sci. 63, 1831–1851. https://doi.org/10.1007/s11430-019-9626-5.